Numerical Investigation and Optimization of a Flushwall Injector for Scramjet Applications at Hypervelocity Flow Conditions

Rajiv R. Shenoy,[†] Tomasz G. Drozda,[‡] Erik L. Axdahl,[‡] and Robert A. Baurle,[‡]
NASA Langley Research Center, Hampton, VA 23681

ABSTRACT

An investigation utilizing Reynolds-averaged simulations (RAS) was performed in order to find optimal designs for an interdigitated flushwall injector suitable for scramjet applications at hypervelocity conditions. The flight Mach number, duct height, spanwise width, and injection angle were the design variables selected to maximize two objective functions: the thrust potential and combustion efficiency. A Latin hypercube sampling design-of-experiments method was used to select design points for RAS. A methodology was developed that automated building geometries and generating grids for each design. The ensuing RAS analysis generated the performance database from which the two objective functions of interest were computed using a one-dimensional performance utility. The data were fitted using four surrogate models: an artificial neural network (ANN) model, a cubic polynomial, a quadratic polynomial, and a Kriging model. Variance-based decomposition showed that both objective functions were primarily driven by changes in the duct height. Multiobjective design optimization was performed for all four surrogate models via a genetic algorithm method. Optimal solutions were obtained at the upper and lower bounds of the flight Mach number range. The Kriging model obtained an optimal solution set that predicted high values for both objective functions. Additionally, three challenge points were selected to assess the designs on the Pareto fronts. Further sampling among the designs of the Pareto fronts are required in order to lower the errors and perform more accurate surrogate-based optimization.

INTRODUCTION

The design of fuel injector systems, fuel-air mixing, and efficient combustion and flameholding are key fluid dynamic challenges for optimal designs of scramjet flowpaths. Attempts to enhance the fuel-air mixing, while simultaneously reducing total pressure losses, thereby improving thrust potential, have received a great deal of attention over the years.[1] Although a certain amount of total pressure loss is expected due to the desired effect of molecular mixing of the fuel and air, further losses will reduce the thrust potential of the engine and should, therefore, be minimized.

[†]Research Engineer, Analytical Mechanics Associates, Inc.
[‡]Research Aerospace Engineer, Hypersonic Airbreathing Propulsion Branch

The Enhanced Injection and Mixing Project (EIMP) being conducted at the NASA Langley Research Center, represents an effort to achieve more rapid mixing at high speeds.[2] The EIMP aims to investigate scramjet fuel injection and mixing physics, improve the understanding of underlying physical processes, and develop enhancement strategies relevant to flight Mach numbers greater than 8. Since a shorter combustor results in a lighter vehicle, the ultimate goal is to minimize the overall combustor length, while producing sufficient thrust and minimal losses. Furthermore, it is beneficial to obtain functional relationships between the relevant performance metrics, such as combustion efficiency and losses, and the flowpath geometrical parameters, such as spanwise spacing, in order to guide design changes. In the experiments, which are underway in the Arc-Heated Scramjet Test Facility (AHSTF), various fuel injection devices are being tested on an open flat plate located downstream of a Mach 6 facility nozzle, which simulates the combustor entrance flight enthalpy of a flight vehicle traveling at a Mach number of about 14 to 16. An open flat plate geometry was chosen, as opposed to a closed duct, in order to facilitate optical access for nonintrusive diagnostics and to simplify the experiment. Furthermore, the tests are conducted at reduced total temperature and with an inert fuel simulant (helium) to allow for uncooled test hardware, thereby further reducing the complexity and cost of the experiment. The impact of reduced total temperature, inert fuel simulant, and open plate versus ducted flowpath configuration on the mixing character of the flow has been previously assessed computationally.[3,4] The mixing performance of three baseline fuel injectors: a strut, a ramp and a flushwall, under these experimental conditions, has been characterized computationally.[5] The effect of varying the flight Mach number between 8 and 15 was investigated subsequently for these baseline fuel injectors.[6] The goal of the present study is to perform optimization of an interdigitated flushwall injector in a straight duct, using hydrogen as the fuel. Surrogate models, which will be trained or developed using Reynolds-averaged simulations (RAS), are used by a genetic algorithm to drive optimization in order to substantially reduce computational expense.

INJECTOR GEOMETRY AND FLOW CONDITIONS

Top and side views and dimensional details of the flushwall injector geometry are shown in Fig.1. The port's exit interface shape is derived from the multiobjective optimization work of Ogawa.[7] The flushwall injector introduces a number of flow features around the injection site that interact to produce a fluidic blockage. A bow shock forms upstream of the injection plume creating total pressure losses and aerodynamic blockage by forcing the air to flow around the fuel plume. The fuel plume entering the high-speed crossflow generates a counterrotating vortex pair, which becomes the main mechanism for stirring the fuel into the air. However, unlike a fuel placement device, such as a strut, the extent to which the fuel penetrates into the airflow is governed by fluidic considerations.[1,8–10] The jet penetration has been shown to be primarily proportional to the ratio of the orthogonal components of the dynamic pressure (or momentum flux) of the main air and the fuel jet, and is further enhanced by matching the static pressure at the exit of the fuel injector to the static pressure of the air just upstream of the fuel plume and downstream of the bow shock. The injector port has a rectangular cross section with the longer dimension aligned with the streamwise direction. Ogawa[7] showed that a high aspect ratio oval cross-section port was desirable for high mixing efficiency and fuel penetration. The injection angle α, i.e., the angle of the port with respect to the streamwise direction, is variable and the port rotates about an axis coinciding with the intersection of the upstream port wall and the combustor plate as detailed in Fig.1. The injector also contains an expansion section with a 6 degree half-angle. The port's width is fixed at 0.1392 inches and the port's throat height is 0.1541 inches. The expansion area ratio is approximately 2.95 with an exit height of 0.4551 inches. The interface created as the port is rotated about the rotation axis varies with the injection angle. This interface has length L, which is equivalent to the port's exit height when $\alpha = 90^\circ$.

Figure 2 shows a schematic view of the flow cross section for the interdigitated flushwall injector configuration. An infinite row of interdigitated injectors is simulated. The duct height h is defined as the distance between the two combustor plates, while the spanwise spacing w is defined as the distance between two injector ports attached to the same plate. The intended fueling area (IFA) is defined as the portion of the cross-sectional area of the duct that each injector is expected to fuel independently of others, demarcated

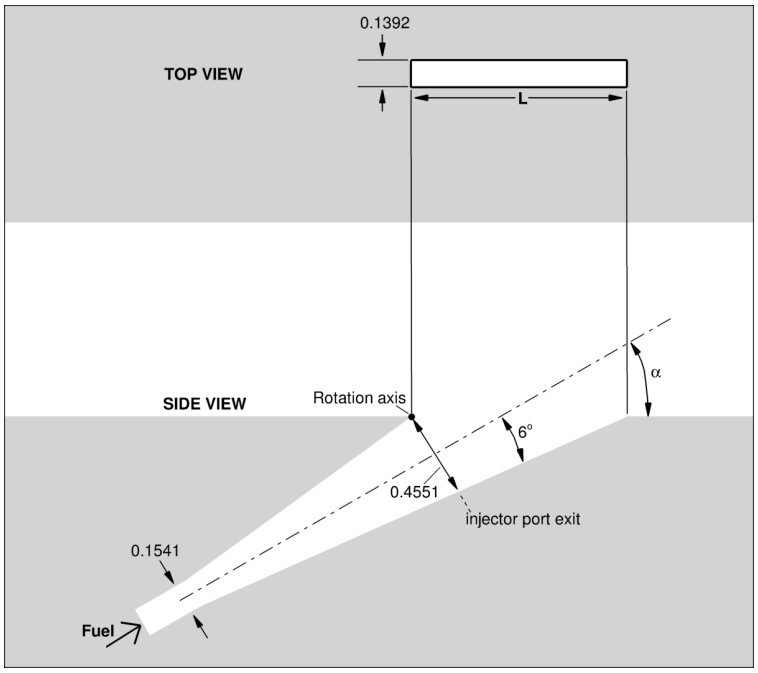

Figure 1. Dimensional details of the baseline flushwall injector (dimensions are in inches). The injection angle is denoted as α. The injector port intersects the combustor plate across an interface with length L.

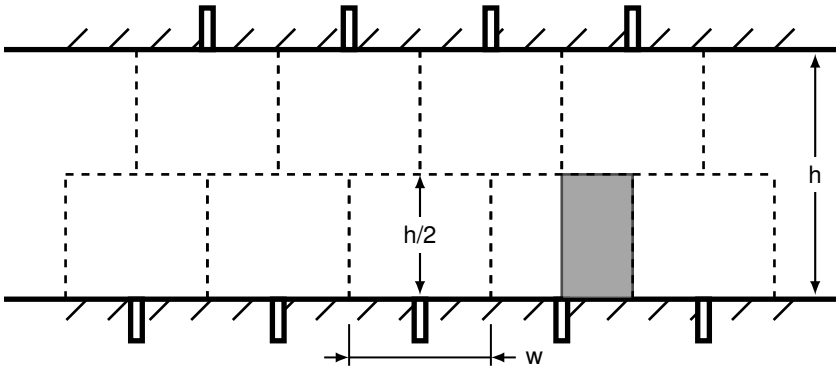

Figure 2. Schematic of the cross-section view of the ducted flowpath with a row of interdigitated flushwall injectors The region between dashed lines denote the IFA for each injector and the shaded area illustrates the cross-section of the computational domain used.

by dashed lines. For the flushwall injector, an appropriate choice for the IFA is the half-height times the spanwise spacing ($h/2 \times w$).

The flight conditions of interest in this study range from a Mach number of 8 to 15 assuming a nominal vehicle flight path along a constant dynamic pressure trajectory of 1500 psf. The freestream air is then compressed to 50.66 kPa with an inlet model assuming 95% isentropic efficiency and 99% adiabatic efficiency. The kinetic energy efficiency of this notional inlet is about 98%. The total inlet contraction ratio ranges from about 7.3 at a flight Mach number of 8 to about 20.0 at a flight Mach number of 15. The combustor inflow Mach number ranges from about 3.7 to 6.4 as the flight Mach number varies from 8 to

15, respectively. The freestream conditions for flight Mach numbers of 8 and 15 are shown in Table 1. The combustor flowpath entrance static pressure was maintained 50.66 kPa (half an atmosphere) for all flight conditions. A thermally perfect mixture of 21% oxygen (O_2) and 79% nitrogen (N_2) by volume was used for the air. Hydrogen fuel is supplied at a total temperature of approximately 1200 K and its mass flow rate for each injector was computed based on an equivalence ratio (ER) of 0.75 over the IFA.

OBJECTIVE FUNCTIONS OF INTEREST AND DESIGN VARIABLES

The performance of the fuel injection was evaluated using two metrics of interest, which were selected from a number of different metrics that are typical in such combustion performance analyses.[11] The first metric of interest is the thrust potential. This metric is obtained by expanding one-dimensional values of the flow variables at each streamwise location through an ideal (isentropic) thrust nozzle. In the current work, this (thermodynamic) expansion process is evaluated until the flow reaches the static pressure at the combustor flowpath entrance. The thrust potential is computed from:

$$\overline{TP} = \dot{m}_e u_e + p_e A_e - \dot{m}_i u_i - p_i A_i \tag{1}$$

where TP is the stream thrust potential (not net thrust potential); $\dot{m}$, u, p, and A, are the mass flow rate, velocity, static pressure, and the area, with subscripts e and i denoting conditions at the thrust nozzle exit plane, and the flowpath entrance (inflow), respectively. The stream thrust potential only includes the internal portion of the flowpath as the control volume, whereas the net thrust potential includes the entire notional flowpath in its formulation. Since the mass flow rate through the flowpath varies with the flight condition and the IFA is unique to each injector, it is beneficial to normalize the thrust potential based on an inflow mass flow rate that is processed by each combustor in order to draw useful comparisons as the flight condition changes. The resulting mass-flow specific stream thrust potential is:

$$TP_m \equiv \frac{\overline{TP}}{\dot{m}_i} = \frac{\dot{m}_e u_e + p_e A_e - p_i A_i}{\dot{m}_i} - u_i. \tag{2}$$

This metric represents an ideal potential mass-flow specific stream thrust that could be obtained when a flowpath of interest is truncated at a given streamwise location and coupled at that location to an ideal thrust nozzle. However, the flow in the thrust nozzle is assumed to be chemically "frozen" starting at the point of expansion, and therefore, this metric does not account for any additional mixing (thrust loss) and reaction (thrust gain) during the expansion process. For the rest of this paper, this mass-flow specific stream thrust potential will be referred to as the thrust potential for brevity (TP_m). All of the losses in the value of the total pressure still appear as a decrease in the value of the thrust potential, however, the chemical reactions, which energize the flow, could increase the value of the thrust potential.

The second metric to serve as an objective function of interest is the combustion efficiency, which quantifies how completely a given flowpath is able to process a mixture of fuel and air into combustion products, thereby enabling heat release into the flow. The combustion efficiency is selected in this work in addition to the thrust potential in order to incorporate designs that promote fuel mixing (and, thereby, combustion) as desirable, rather than designs that simply augment thrust with added momentum of the unmixed fuel and/or designs that do not generate significant heat release that helps to augment thrust. There exists a number

Table 1. Freestream conditions for the extrema of flight Mach numbers in the current simulations.

Alt. (km)	Mach No.	Q (kPa)	p (kPa)	T (K)	T_0† (K)	p_0† (MPa)
28.0	8.0	71.82	1.6048	232.4	2753.9	24.78
36.6	15.0	71.82	0.4565	249.4	8816.6	1333.2

†Value based on frozen composition of air

of combustion efficiency definitions, however, in this effort, the simplest definition based on the fuel mass fraction depletion is used, i.e.,

$$\eta_c = 1 - \frac{\dot{m}_f}{\dot{m}_{f,tot}} \tag{3}$$

where $\dot{m}_f$ and $\dot{m}_{f,tot}$ are the integrated mass flow rates of fuel at a streamwise location of interest and the total injected fuel flow rate, respectively.

Four parameters are used as design variables. These are the flight Mach number M, duct height h, spanwise spacing w, and the injection angle α. The bounds of these variables were chosen based on results obtained from previous work and problem feasibility. The optimization problem can be characterized as follows:

maximize:	thrust potential: TP_m
	combustion efficiency: η_c
subject to:	flight Mach number: $8.0 \leq M \leq 15.0$
	duct height: $1.0 \leq h \leq 3.0$
	spanwise spacing: $0.8 \leq w \leq 2.0$
	injection angle: $30^\circ \leq \alpha \leq 90^\circ$

Both optimization quantities are obtained at the exit of the domain, i.e., 25 inches downstream of the fuel injection plane. The flight Mach number bounds reflect the flight conditions of interest from previous work,[6] while the duct height and spanwise spacing bounds are selected based on estimates of where optimal solutions are expected. The injection angle bounds were selected based on the optimization effort of Ogawa.[7]

COMPUTATIONAL METHODOLOGY

The numerical simulations were performed using the Viscous Upwind aLgorithm for Complex flow ANalysis (VULCAN-CFD) code.[12] VULCAN-CFD is a cell-centered, finite-volume solver widely used for high-speed flow simulations. For this work, Reynolds-averaged simulations (RAS) were performed using structured, multiblock grids. The advective terms were computed using the Monotone Upstream-Centered Scheme for Conservation Laws (MUSCL) scheme[13] with the Low-Dissipation Flux-Split Scheme (LDFSS) of Edwards.[14] The thermodynamic properties of the mixture components were computed using the curve fits of McBride et al.[15] The governing equations were integrated using an implicit diagonalized approximate factorization (DAF) method.[16] The current work used the Menter Baseline two-equation turbulent physics model.[17] The Reynolds heat and species mass fluxes were modeled using a gradient diffusion model with turbulent Prandtl and Schmidt numbers of 0.9 and 0.5, respectively. The chemical reactions are modeled using the nine-species / nineteen-reaction hydrogen air kinetic model of Ó Conaire and Westbrook,[18] with turbulent-chemistry interactions not modeled. Wilcox wall matching functions[19] were also used, however, their implementation in VULCAN-CFD includes a modification that allows the simulations to recover the integrate-to-the-wall behavior as the value of normalized wall-distance, y^+, approaches one. All simulations were converged until the total integrated mass flow rate and the total integrated heat flux on the walls remained constant to at least 4 decimal points. This typically occurred when the value of the L_2-norm of the steady-state equation-set residual decreased by about 3–4 orders of magnitude. To conserve the available computational resources, all the simulations were split into elliptic and space-marching regions. The elliptic region contained the inflow of the domain, the injector bodies, and up to 6.5 inches downstream of the injection plane. The computational cell count was about equal in both regions, but the computational cost associated with solving the space-marching region was about an order of magnitude lower than that for the elliptic region. Past experience for similar interdigitated injector configurations have shown that this approach accurately simulates the flow features and integrated values from the one-dimensional metrics of interest when compared against simulations obtained from using a single, fully elliptic region.[6]

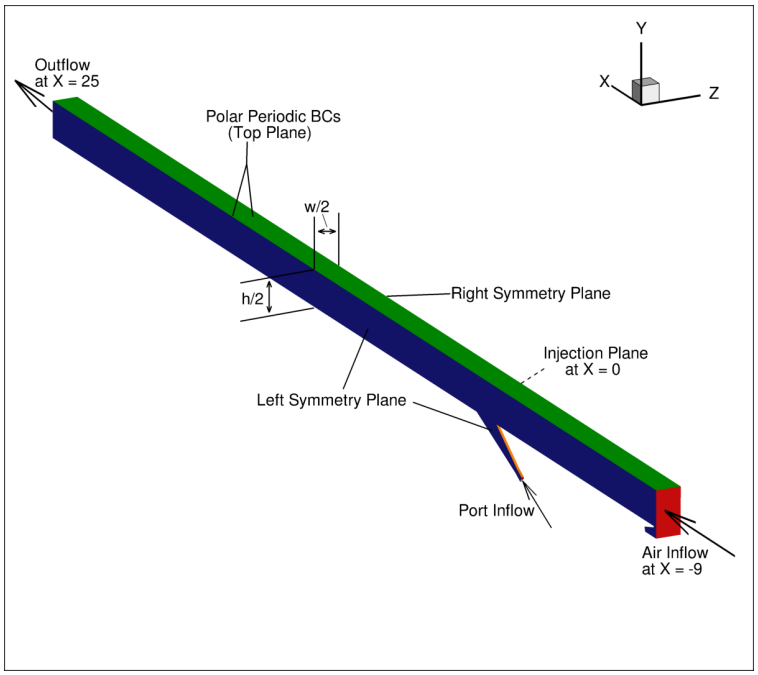

(a) View showing entire combustor with relevant boundary conditions and streamwise stations.

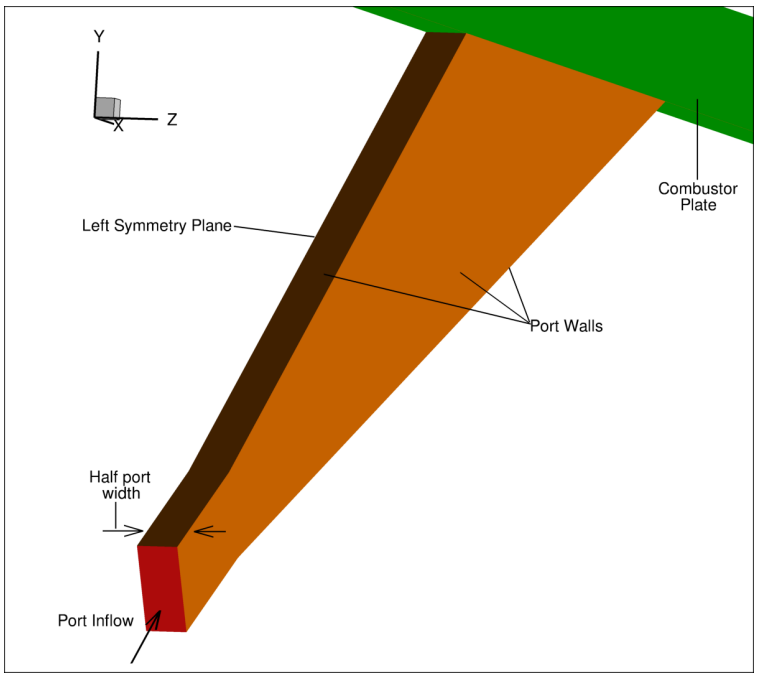

(b) Detailed view of injector port and combustor plates.

Figure 3. Computational domain of the combustor with relevant details. All dimensions are in inches.

The computational domain for these interdigitated flushwall injectors is illustrated in Fig. 3. The inflow and outflow planes are placed at 9 inches upstream and 25 inches downstream, respectively, of the fuel injection plane, which is located at X = 0. The left symmetry plane bisects the port laterally and the right symmetry plane is coincident with the plane halfway between adjacent injectors ports intersecting the same plate.

These lateral symmetry planes are $w/2$ apart. The interdigitated symmetry is taken advantage by placing a pair of polar periodic boundary conditions at $h/2$ above the bottom combustor plate (halfway to the top plate). The cross-sectional area of the computational domain corresponds to half the IFA and is shaded in gray in Fig. 2.

Efficient sampling of the design space was accomplished by utilizing DAKOTA's Latin hypercube sampling (LHS).[20] The LHS is a design-of-experiments (DoE) method that generates space-filling samples over a multidimensional design space. Here, fifty samples were chosen to cover the entire design space over the four design variables. Additionally, sixteen corner points of the four-variable hypercube were also chosen to anchor the surrogate models and improve accuracy near the corners. A computational grid dependence study was previously conducted by Drozda et al.[5] showing that a nominal spacing of 0.01 inches obtained sufficiently low errors (approx. 5%) for total pressure recovery and mixing efficiency.

Geometries and grids for these DoE simulations were generated using the GoHypersonic Inc., LINK3D software,[21] which enables efficient, parallel grid generation that is amenable to geometric modifications and design optimization. A methodology was developed that automatically generates the required geometry and performs grid smoothing and clustering based on the geometrical design parameters of each case in the DoE. First, using the geometric design variables, i.e., the duct height, spanwise spacing, and injection angle, geometry curves and surfaces are generated. Since topology nodes reside in one-dimensional and two-dimensional coordinates with respect to their associated geometry curves and surfaces, respectively, the nodal locations can be automatically updated in response to a geometric modification. This allows for the same topology to be used for all the geometries in the DoE. The second step involved assigning dimensions for a small group of edge families in the topology so that a nominal spacing of 0.01 inches was achieved. Finally, the grids, which ranged between 4.8 million cells to 23.8 million cells, were smoothed and clustered using LINK3D's parallel grid engine on a desktop machine, typically in one hour. Figure 4 shows slices of the grid at the left symmetry plane for two different geometric configurations from the DoE. While the first case has a small injection angle and a large duct height, the second has a large injection angle and a smaller height.

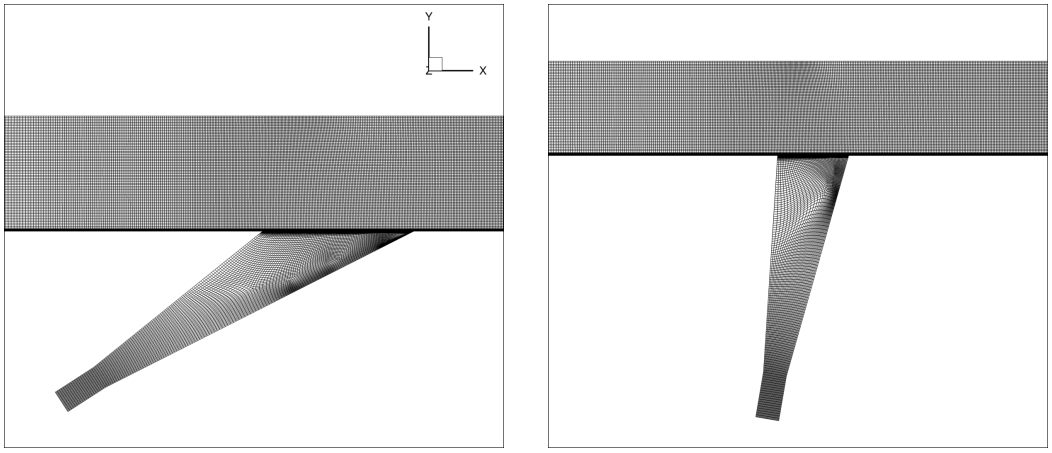

(a) Case with $h = 1.5266$ and $\alpha = 32.892°$.

(b) Case with $h = 1.2497$ and $\alpha = 80.261°$.

Figure 4. Grid slices at the left symmetry plane foe two DoE configurations.

RESULTS AND DISCUSSION

The responses of the two objective functions, i.e., the thrust potential and the combustion efficiency, are plotted against the different design variables for the fifty (interior) DoE points in Fig. 5. Although these responses are functions of four independent variables, they are plotted as projections over two-dimensional space for convenience in visualization as well as to highlight the main effects due to changes in the individual design variables. These responses are plotted in the form of scatter plots as well as being interpolated onto a two-dimensional grid. The left column shows plots of the thrust potential, while the right column displays the combustion efficiency. The duct height is shown as a variable in all plots because the data indicated that both objective functions were strongly influenced by this variable. Increasing duct height tends to increase the thrust potential, while decreasing it tends to increase the combustion efficiency. Both objective functions show desirable values over a wide range of height values, suggesting that duct height can be a variable of compromise. Desirable values of the thrust potential can be found at both the lower and higher ends of the flight Mach number spectrum, while desirable values of combustion efficiency can be found over the full range of flight Mach numbers for lower values of duct height. As the injector angle increases, the thrust potential tends to decrease and the combustion efficiency tends to increase. This is expected since aligning the flow closer to the air stream (i.e., when the injector angle is low) would contribute more streamwise momentum, whereas directing the fuel in a more transverse fashion to the air stream would promote more mixing (and thereby combustion) by increasing fuel penetration. High injection angles, however, decrease the thrust due to minimal axial fuel injection while increasing the total pressure losses due to stronger bow shocks, which offset the thrust gains from heat release obtained from increased combustion efficiency. Varying the spanwise spacing produced multiple maxima for the thrust potential and desirable values of combustion efficiency over the entire spanwise spacing range, when the duct height is small. The spanwise spacing appears to be less influential when compared against the other design variables.

Four different surrogate models are applied to fit the data using DAKOTA's surrogate model capabilities. These are the quadratic and cubic polynomial models, the Kriging or Gaussian process model with a reduced quadratic trend option, and the artificial neural network (ANN) model. The models are fitted to approximate both objective functions and root-mean-squared errors are computed. These errors, listed in Table 2, are computed by two methods: residuals and 10-fold cross-validation. The residual method obtains the deviation of the observed data from the model's predictions using the full set of training data. Cross-validation (CV) is a technique used to predict how well a model performs when tested against unseen data. Using 10-fold CV, the training data is randomly divided into ten partitions. For each partition, the data set of the partition is reserved for validating a model, which is computed using the data set from the remaining nine partitions. In this way, ten separate models are computed for the ten partitions. The errors of these ten models are averaged to compute the CV error metric. The residual errors are similar between the ANN and quadratic polynomial models, and are lower for the cubic polynomial model. The Kriging model, by definition, will have zero residual error. Using the 10-fold CV method, the ANN and cubic polynomial models perform the worst, while the Kriging model exhibits the least error.

Table 2. Root-mean-squared errors for the different surrogate models.

	Residual		10-fold CV	
	TP_m	η_c	TP_m	η_c
ANN	21.9	0.043	46.4	0.071
Cubic	12.8	0.031	43.7	0.102
Kriging	-	-	25.4	0.057
Quadratic	21.0	0.044	32.2	0.059

The coefficients of the polynomial bases for the cubic, quadratic, and Kriging models are plotted in Fig. 6 in order to assess the sensitivity of the models to varying the number of samples required to generate the model. The cubic polynomial fit's coefficients for both the thrust potential and combustion efficiency appear to change with increasing samples, suggesting that a larger number of samples are required to

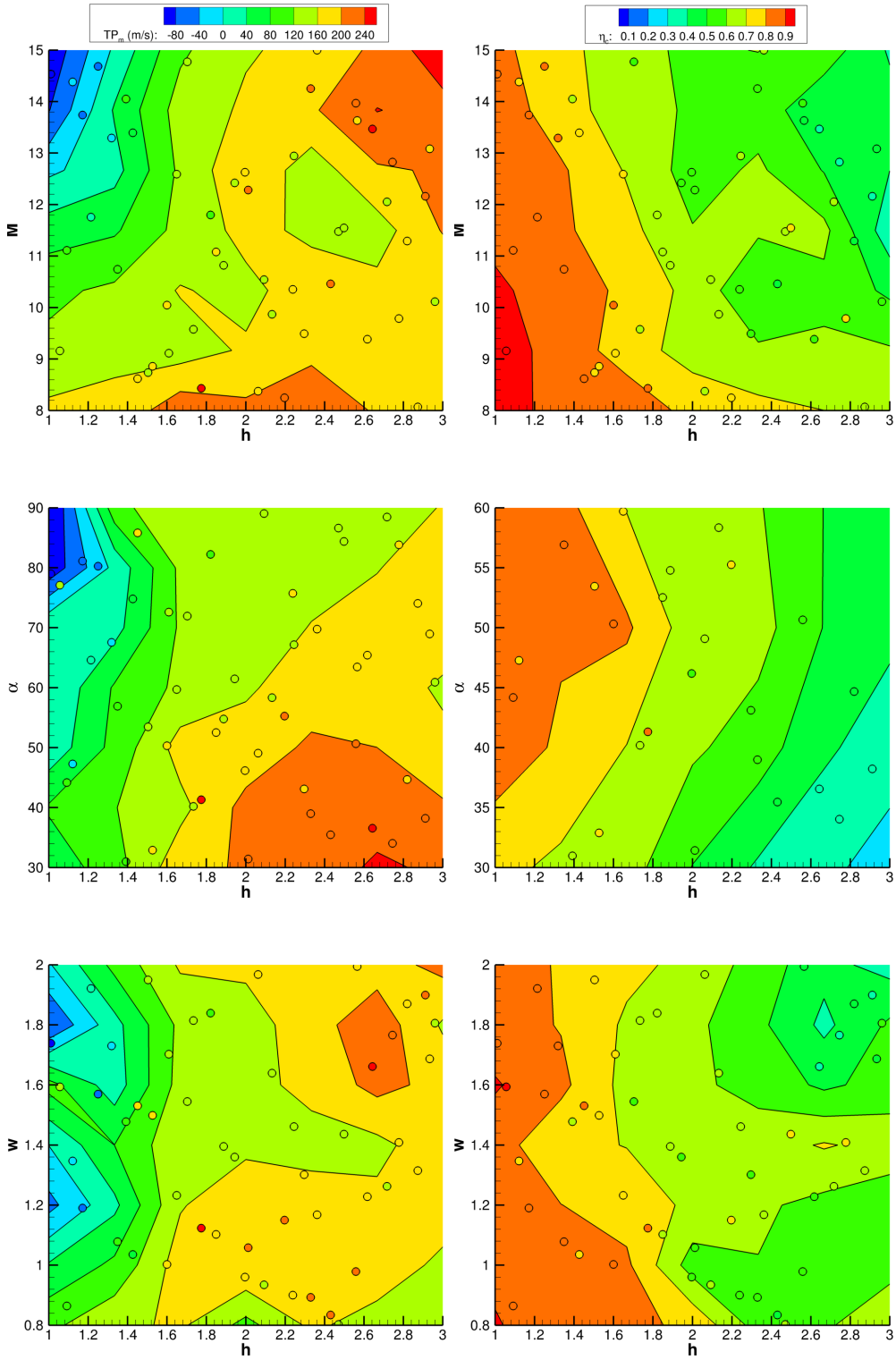

Figure 5. Variations of both objective functions in response to different combinations of design variables.

generate an accurate response model. The coefficients for the quadratic fit for the thrust potential appear to be insensitive to adding new samples after around 55 samples, while some of the coefficients for the combustion efficiency still change by small amounts as samples increase. The Kriging model's coefficients appear more sensitive to the number of samples for the thrust potential than for the combustion efficiency, although more samples may be required before the model is insensitive to addition of new samples.

DAKOTA enables sensitivity assessment using variance-based decomposition, which is a global sensitivity analysis method that gives a measure of how a model's variability can be attributed to variations in individual input design variables.[20] Variance-based decomposition utilizes the first-order sensitivity index S_i and the total-effect index T_i, also known as Sobol indices. The fraction of the variability in the output, Y, that can be attributed solely to an individual input variable, x_i, is described by the first-order sensitivity index, while the total-effect index describes the fraction of the variability in the output that can be attributed to a given input variable as well as its interactions with other variables. The formulas for these indices are:

$$S_i = \frac{Var[E(Y|x_{\sim i})]}{Var(Y)} \tag{4}$$

and

$$T_i = \frac{E[Var(Y|x_{\sim i})]}{Var(Y)} = \frac{Var(Y) - Var[E(Y|x_{\sim i})]}{Var(Y)} \tag{5}$$

where $x_{\sim i}$ denotes the set of all input variables except x_i. Using the four different surrogate models, Sobol indices are computed and plotted in Fig. 7. It is noticeable that the duct height has a major influence on both the thrust potential and combustion efficiency. The flight Mach number and injection angle have a secondary influence on both objective functions, while the spanwise spacing has the least significant influence. The models do not show significant deviation from one another except for the quadratic polynomial fit of the thrust potential, where the spanwise spacing appears even less influential than for the other surrogate fits. The total-effect indices for the thrust potential are significantly greater than their first-order counterparts indicating that the design variables have interactional effects that contribute to the thrust potential output. Specifically, it is clear that the total-effect indices of the duct height and flight Mach number are greater than their first order indices. As observed in Fig. 5, for a low duct height and a higher flight Mach number, thrust potential is low, whereas, for higher values of duct height and lower values of flight Mach number, thrust potential is generally high. Unlike, the thrust potential, the total-effect indices for the combustion efficiency show smaller interactional effects from the design variables, suggesting that these variables, in comparison, are relatively independent in affecting this output.

Multiobjective design optimization is performed using these four surrogate models using DAKOTA's multiobjective genetic algorithm. The algorithm starts with a randomly generated population over the design space using the surrogate model, instead of CFD, to obtain objective function responses. The best design points are then allowed to survive over several generations by performing crossover and mutation operations, and assessing the fitness of each member in the population. The algorithm is terminated when a convergence criteria is met. In this effort, an initial population size of 100 is selected and reproduction requires that two parents generate two offspring. The crossover and mutation rates are set to 0.8 and 0.1, respectively.

Figure 8 (a) shows the final populations of nondominated solutions from the four different surrogate models. For the two objective functions, TP_m and η_c, a nondominated solution means that no further improvement of one function was found without a tradeoff from the other function. The set of these nondominated solutions obtained from each model is also known as a Pareto front. The plots also show the interior points obtained from the LHS DoE method marked by open circles as well as the sixteen corner points of the hypercube marked by plus signs (+). The Pareto fronts resulting from the different models show discontinuities, which result due to the generation of concave sections of the objective function fronts during the genetic algorithm iterations. These concave sections contain solutions that are dominated by other (nondominated) solutions for both objective functions. The quadratic and cubic polynomial models show optimal designs that obtain combustion efficiencies greater than one, which is nonphysical. This is because the surrogate models applied were not constrained by known physical limits. This modeling shortcoming could indicate possible model underfitting or that the utilization of physical constraints within the model is necessary for an accurate

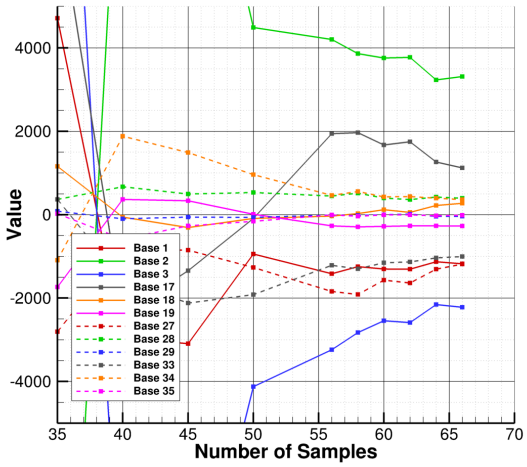

(a) Cubic polynomial coefficients for TP_m.

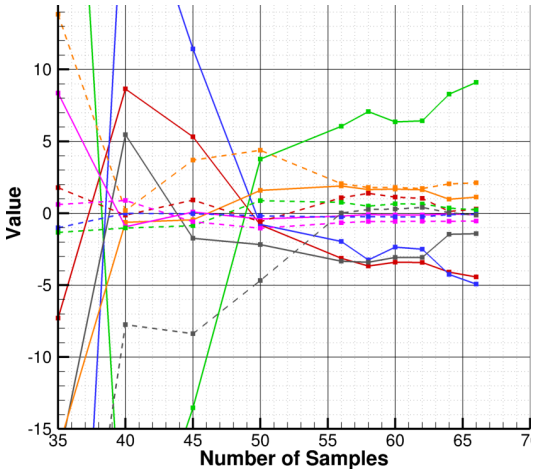

(b) Cubic polynomial coefficients for η_c.

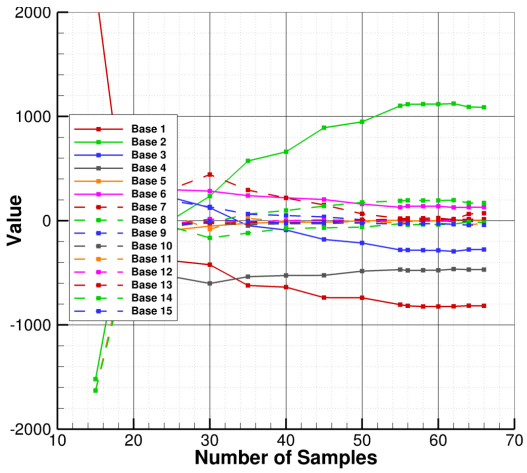

(c) Quadratic polynomial coefficients for TP_m.

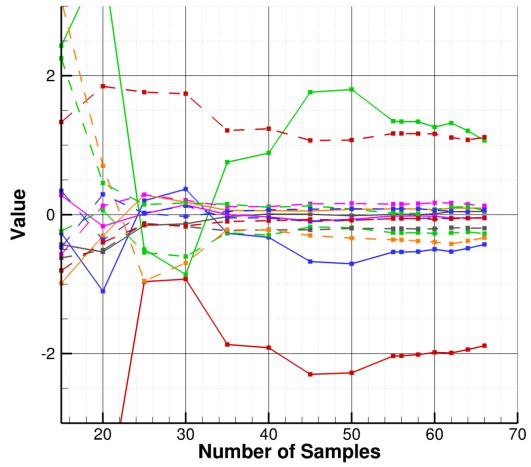

(d) Quadratic polynomial coefficients for η_c.

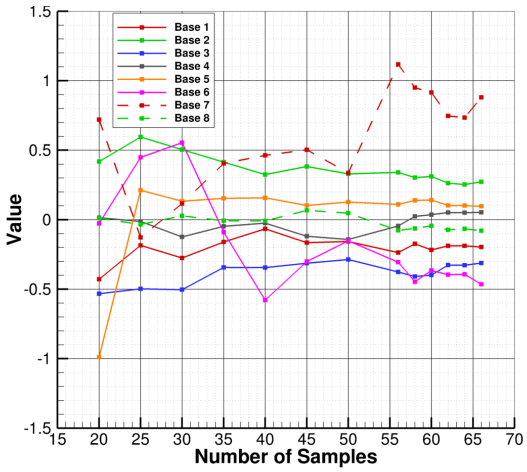

(e) Kriging coefficients for TP_m.

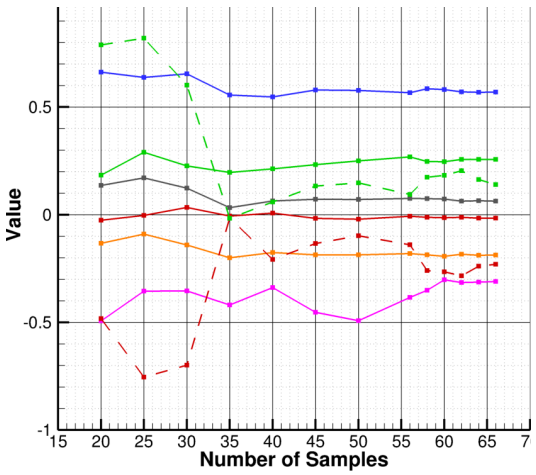

(f) Kriging polynomial coefficients for η_c.

Figure 6. Variation of the model coefficients in response to varying the number of samples.

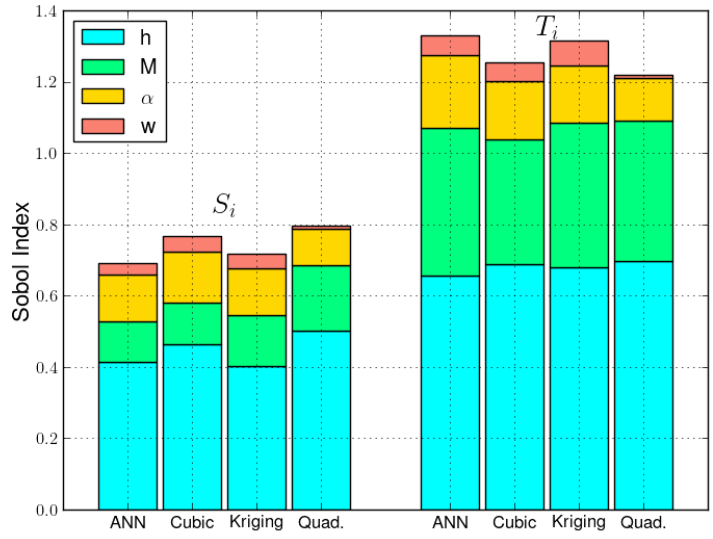

(a) First-order and total-effect indices for TP_m

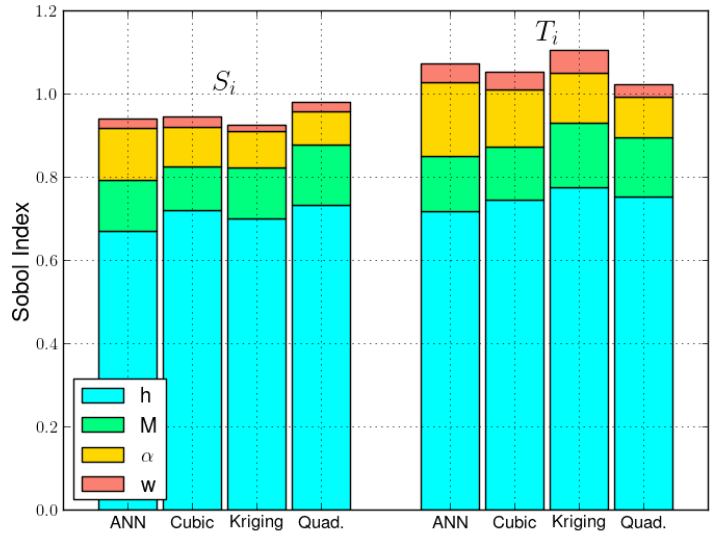

(b) First-order and total-effect indices for η_c

Figure 7. Sensitivity indices computed for the different surrogate models for the effect of design variables on the two objective functions.

fit. The Pareto front resulting from the ANN and quadratic model results in designs that are suboptimal than two designs from training data, which have values of thrust potential and combustion efficiency of approximately 245 m/s and 0.90, respectively. Unlike the cubic and Kriging models, these models did not fit these training data adequately, resulting in suboptimal Pareto fronts. The ANN, cubic, and quadratic models all show a similar clustering of the Pareto front region where thrust potential is high (between approx. 250 m/s and 310 m/s) and combustion efficiency is low (between approx. 0.4 and 0.5). The Kriging model yields an interesting solution set for the Pareto front, where both the thrust potential and combustion efficiency are high, that is not predicted by the other three models. The variance in the ranges of these Pareto fronts illustrate that further iterations of sampling and optimization are warranted.

Figures 8 (b)–(e) show the same Pareto fronts and training data with symbols colored by the design variables. The four models show that optimal solutions arise for the upper and lower flight Mach number

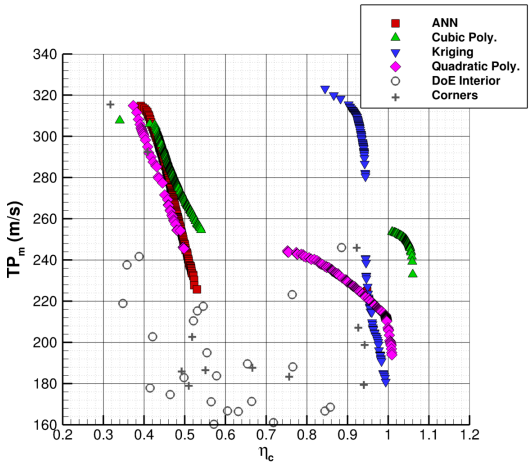

(a) Comparison of the solutions from different models.

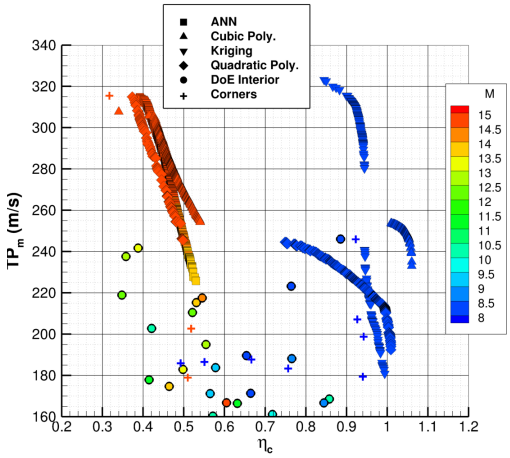

(b) Solutions with symbols colored by flight Mach number.

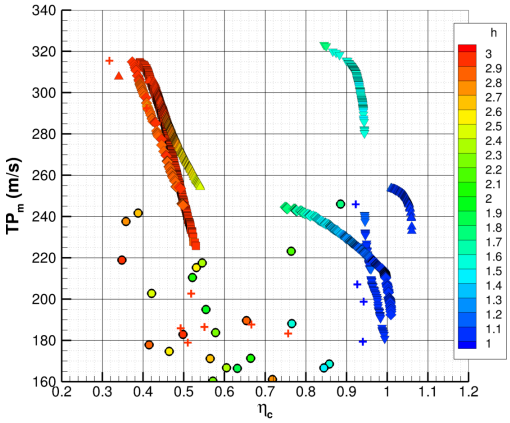

(c) Solutions with symbols colored by duct height.

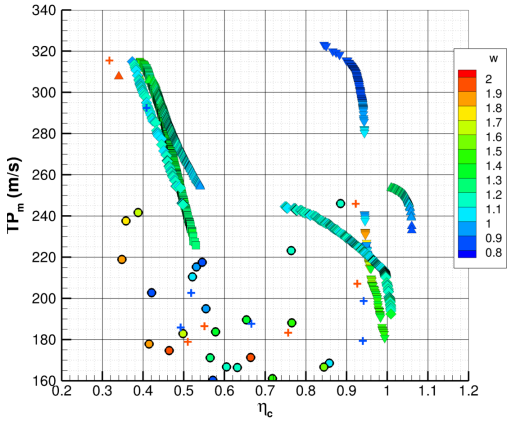

(d) Solutions with symbols colored by spanwise spacing.

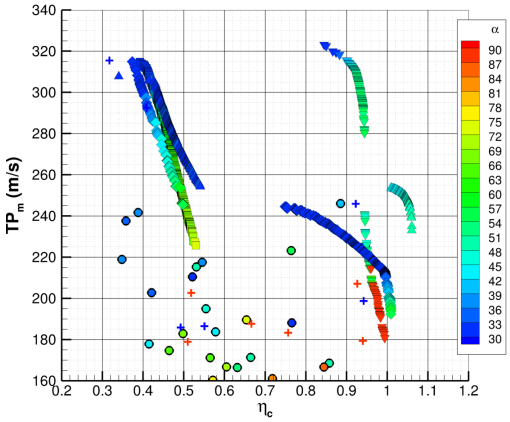

(e) Solutions with symbols colored by injection angle.

Figure 8. Optimization solutions and training data with the different surrogate models obtained from the final population of the optimization algorithm.

limits, except the ANN model, which shows only a small range of Mach numbers close to the upper end. The duct height for these optimal solution sets are similar for the ANN, cubic, and quadratic models, where low duct height results in optimal solutions that yield high combustion efficiency at the expense of thrust potential (in the southeast region of the plot), and high duct height results in optimal solutions that yield high thrust potential at the expense of combustion efficiency (in the northwest region of the plot). The Kriging solutions show that over the middle range of the duct height, high values of both the thrust potential and combustion efficiency are predicted. The spanwise spacing values are in the middle range for the optimal solutions resulting from the ANN, cubic, and quadratic model, whereas for the Kriging model, low values of spanwise spacing yields high thrust and high combustion efficiency. The injection angle values vary from low values to midrange values for the optimal solutions resulting from the ANN, cubic, and quadratic models, while the Kriging solutions show the full range of the injection angle values. As expected, the lower the injection angle, the higher the resulting thrust potential, whereas the higher the injection angle, the higher the combustion efficiency and lower the thrust potential due to greater losses.

In order to assess the accuracy of the Pareto fronts, three challenge design points that were predicted by the cubic and Kriging models were selected so that CFD-generated solutions may be obtained and compared against the predictions given by the models. These challenge points are provided in Table 3. Only the cubic and Kriging models are challenged because these models predicted the greatest improvement with respect to the training data. The first challenge point selected was a point predicted by the cubic model where thrust potential is high and combustion efficiency is moderate. The second challenge point selected was a point predicted by the Kriging model where both the thrust potential and combustion efficiency are high, while the third challenge point selected was a point predicted by the Kriging model where the thrust potential is low but the combustion efficiency very high.

Table 3. Challenge points listed with model prediction and CFD-generated solution. The model challenged is denoted in parentheses.

	Design Variables				Model		CFD	
Point (Model)	M	h	w	α	TP_m	η_c	TP_m	η_c
1 (Cubic)	14.940	2.9690	1.2771	30.312	304.8	0.4286	271.9	0.4308
2 (Kriging)	8.020	1.5160	0.8044	50.298	309.4	0.9234	270.4	0.8913
3 (Kriging)	8.028	1.0740	1.3933	89.940	200.1	0.9753	199.5	0.9156

Confidence intervals were generated by post-processing all 66 training data points using five sets of 10-fold CV analyses. This ensembled CV method enables the generation of 50 surrogate models for each model type that may be sampled over the entire design space. Using the mean and standard deviation of these models evaluated at the solution points of the different Pareto fronts, one can obtain 95% confidence intervals that provide an estimate of the error at these points. It is important to note that these error estimates are obtained by approximating only the training data and, thus, will not be as accurate for points sufficiently far away from the training data. Figure 9 shows the Pareto fronts resulting from the cubic and Kriging models with error bars denoting the 95% confidence interval error estimate. The character X indicates the CFD-generated solution, while the circle highlights the design point on the Pareto front that is being challenged. The first challenge point obtains a good approximation of the CFD-observed value for combustion efficiency, but overpredicts the thrust potential by approximately 32 m/s (nearly 12%). This point falls within its confidence interval estimate. When compared against Fig. 8 (a), this point is close to a corner training data point, where flight Mach number and duct height are at their maximum values and spanwise spacing and injection angle are at their minimum values. The second challenge point falls within the error estimate bounds of combustion efficiency, but is slightly outside of the error bounds of thrust potential. However, it is interesting to note that this point generated high values for both the thrust potential and the combustion efficiency that show improvement in both thrust potential and combustion efficiency with respect to the training data that none of the other models predicted. The third challenge point closely approximates the CFD-observed value for the thrust potential but overpredicts the combustion efficiency by nearly 6% and falls outside of its error bounds.

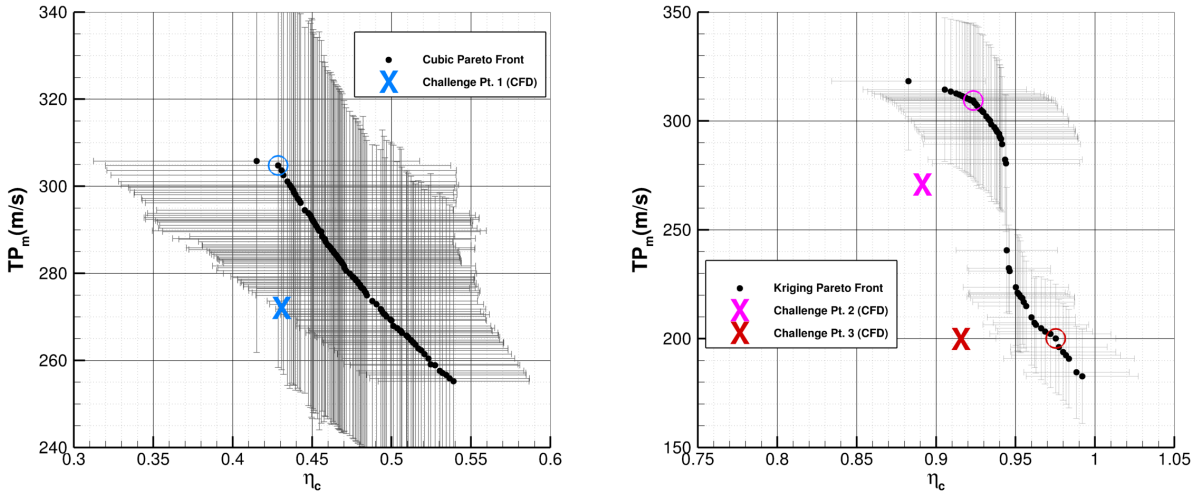

(a) Challenge point 1.

(b) Challenge points 2 and 3.

Figure 9. Comparison of CFD-generated observations at challenge points versus model prediction on Pareto front.

The error estimates given for each of the models based on the available training data are not sufficiently low enough to perform surrogate-based optimization that can accurately deliver optimal designs. In order to drive these errors lower, a set of design points predicted by this first iteration of the optimization would need to be used to augment the training data set, such as those obtained by the challenge point analysis, in order to perform a second optimization iteration. This process may need to be repeated until the surrogate models are sufficiently converged and the optimization yields an accurate representation of the Pareto front.

It is also important to note that the current problem formulation optimizes for the best design point over the flight envelope, i.e., the best flight Mach numbers to fly at along with the best corresponding geometries. This is different from performing optimization over a range of flight Mach numbers. One alternate optimization strategy would be to perform the same optimization over a series of fixed flight Mach numbers in order to obtain a variable geometry that is optimal over this range of flight conditions. Another strategy would be to optimize a fixed geometry across the flight Mach number range, in which for every combination of geometry design variables, maximize the average values of the thrust potential and combustion efficiency over the flight Mach number range. Future efforts will explore such optimization strategies that will enable optimal designs over a range of flight conditions.

Flowfields of the three challenge points are shown in the form of Mach contours in Figs. 10 – 12 in order to highlight the varied physics occuring. The black isolines denote the stoichiometric value of the fuel mass fraction. The design of the first challenge point (Fig. 10) is at the upper bound of the flight Mach number and duct height and lower bound of the injection angle. A relatively high thrust potential is obtained by opening up the duct, which reduces the total pressure losses that result from shock reflections, as well as the low injection angle that augments the fuel in the streamwise direction. A low value of mixing efficiency results due to the fuel not penetrating into the airstream and the fuel plume (denoted by the extent of the black isolines) extending up to the combustor exit. The second challenge point (Fig. 11) occurs at the lower bound of the flight Mach number, moderate duct height, and moderate injection angle. The thrust potential is relatively high because the total pressure losses from the shocks are not as high, allowing a small portion of the flow to have a relatively high Mach number up to the combustor exit. The combustion efficiency is high as the fuel plume mixes well with airstream and depletes well upstream of the combustor exit. The third challenge point (Fig. 12) occurs at the lower bound of the flight Mach number and duct height, and upper

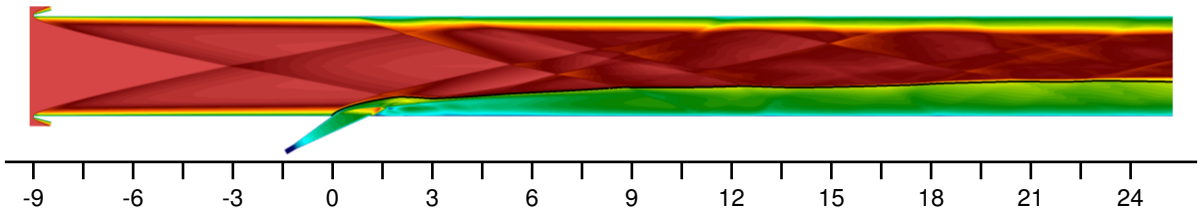

(a) Side view of the port symmetry plane.

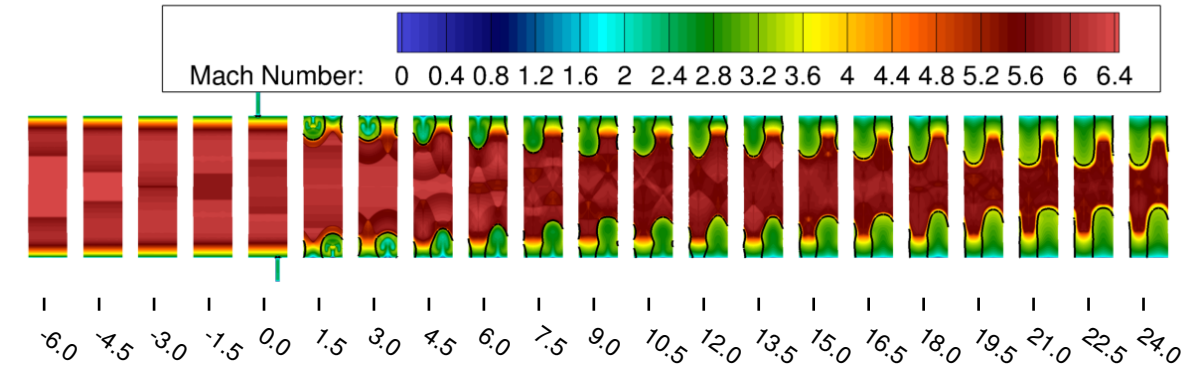

(b) Cross-stream planes.

Figure 10. Mach contours with black isolines denoting stoichiometric value of the fuel mass fraction for challenge point 1.

bound of the injection angle. The small duct height in conjunction with the large injection angle results in lower thrust potential (high total pressure losses) and greater combustion efficiency as fuel depletes further upstream of the combustor exit than for the second challenge point.

SUMMARY AND CONCLUSIONS

A numerical investigation has been conducted in order to find optimal designs for an interdigitated flush wall injector. The flight Mach number, duct height, spanwise spacing, and injection angle are the design variables for optimizing thrust potential and the combustion efficiency of the injector. The training design points were generated using Latin hypercube sampling augmented with the corners of the hypercube. Using a newly developed automated geometry and grid generation methodology, computational grids were efficiently created. The objective functions at the training points were obtained from the resulting Reynolds-averaged simulations using one-dimensional performance metrics. Four surrogate models were obtained to fit the data and error estimates of these models were tabulated. Errors obtained from cross-validation showed that the Kriging model exhibited the least error, while the artificial neural network and the cubic models had the greatest errors. Variance-based decomposition was performed to obtain sensitivity indices. This analysis showed that duct height is the primary driver of both the thrust potential and combustion efficiency. Additionally, the design variables have interactional effects that contribute to the thrust potential response. Multiobjective design optimization was performed using the surrogate models using a multiobjective genetic algorithm. The models showed that optimal solutions are obtained at both the upper and lower flight Mach number limits. The Kriging model resulted in a Pareto front that yielded high values for the both the thrust potential and combustion efficiency that was not captured by the other models. Three challenge points were selected to challenge the optimal solutions predicted by the cubic and Kriging models. The second and third challenge points that assessed the Kriging model did not fall within both objective function's confidence

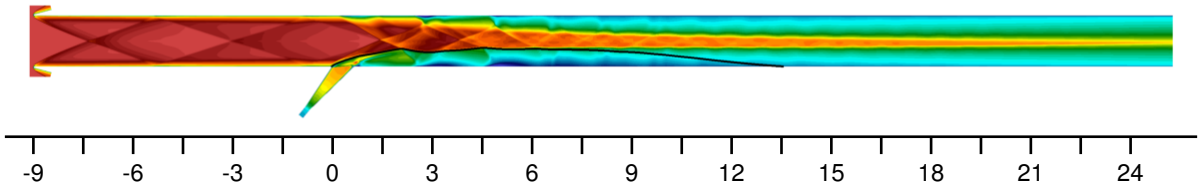

(a) Challenge point 2: Side view of the port symmetry plane.

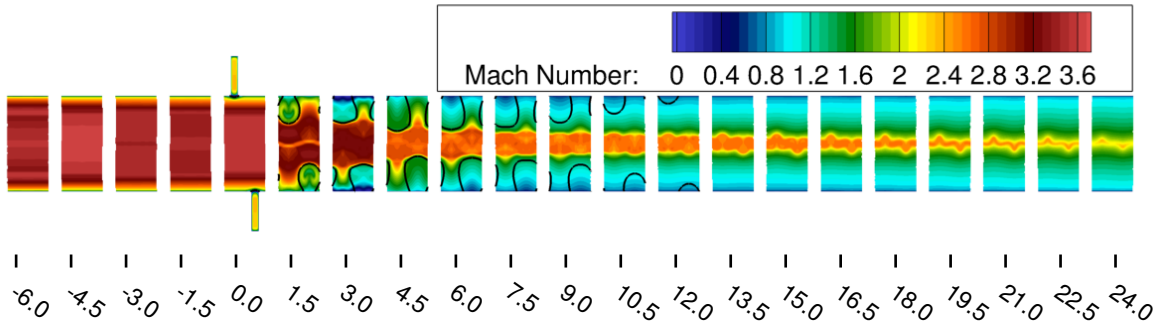

(b) Challenge point 2: Cross-stream planes.

Figure 11. Mach contours with black isolines denoting stoichiometric value of the fuel mass fraction for challenge point 2.

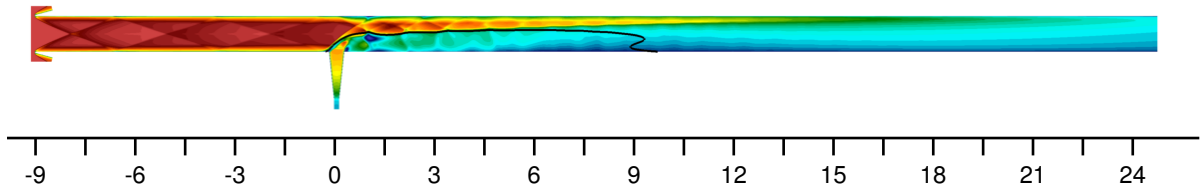

(a) Challenge point 3: Side view of the port symmetry plane.

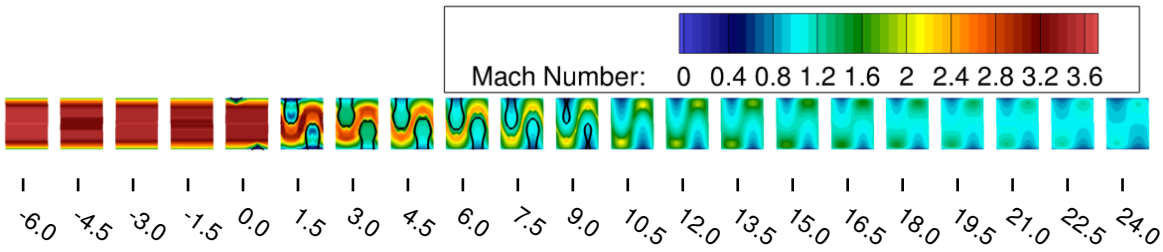

(b) Challenge point 3: Cross-stream planes.

Figure 12. Mach contours with black isolines denoting stoichiometric value of the fuel mass fraction for challenge point 3.

intervals. Further sampling among the designs predicted by the Pareto fronts of these models are warranted in order to drive the error estimates down and perform more accurate surrogate-based optimization.

ACKNOWLEDGMENTS

This work is supported by the Hypersonic Technology Project in the Advanced Air Vehicles Program of the NASA Aeronautics Research Mission Directorate (ARMD). Computational resources are provided by the NASA Langley Research Center and the NASA Advanced Supercomputing (NAS) Division.

REFERENCES

[1] Lee, J., Lin, K.-C., and Eklund, D., ***Challenges in Fuel Injection for High-Speed Propulsion Systems***, AIAA J., 53(6):1405–1423 (Jun. 2015).

[2] Cabell, K., Drozda, T. G., Axdahl, E. L., and Danehy, P. M., ***The Enhanced Injection and Mixing Project at NASA Langley***, in *JANNAF 46th CS / 34th APS / 34th EPSS / 28th PSHS Joint Subcommittee Meeting*, NTRS Report Number NF1676L-25526, Albuquerque, NM (Dec. 2014).

[3] Drozda, T. G., Baurle, R., and Drummond, J. P., ***Impact of Flight Enthalpy, Fuel Simulant, and Chemical Reactions on the Mixing Characteristics of Several Injectors at Hypervelocity Flow Conditions***, in *63rd JANNAF Propulsion Meeting / 47th CS / 35th APS / 345h EPSS / 29th PSHS Joint Subcommittee Meeting*, NTRS Report Number NF1676L-23113, Newport News, VA (May 2016).

[4] Drozda, T. G., Shenoy, R. R., Passe, B. J., Baurle, R., and Drummond, J. P., ***Comparison of Mixing Characteristics for Several Fuel Injectors on an Open Plate and in a Ducted Flowpath Configuration at Hypervelocity Flow Conditions***, in *JANNAF Meeting / 48th CS / 36th APS / 36th EPSS / 30th PSHS Joint Subcommittee Meeting*, NTRS Report Number NF1676L-27197, Newport News, VA (Dec. 2017).

[5] Drozda, T. G., Drummond, J. P., and Baurle, R. A., ***CFD Analysis of Mixing Characteristics of Several Fuel Injectors at Hypervelocity Flow Conditions***, in *52nd AIAA/SAE/ASEE Joint Propulsion Conference*, AIAA 2016-4764, AIAA, Salt Lake City, UT (Jul. 2016).

[6] Shenoy, R. R., Drozda, T. G., Norris, A. T., Baurle, R. A., and Drummond, J. P., ***Comparison of Mixing Characteristics for Several Fuel Injectors at Mach 8, 12, and 15 Hypervelocity Flow Conditions***, in *AIAA Propulsion and Energy Forum*, Cincinnati, OH (Jul. 2018).

[7] Ogawa, H., ***Physical Insight into Fuel-Air Mixing for Upstream-Fuel-Injected Scramjets via Multi-Objective Design Optimization***, J. Propul. Power., 31(6):1505–1523 (2015).

[8] Schetz, J. A. and Billig, F. S., ***Penetration of Gaseous Jets Injected into a Supersonic Stream***, J. Spacecraft. Rockets., 3(11):1658–1665 (1966).

[9] Mao, M., Riggins, D. W., and McClinton, C. R., ***Numerical Simulation of Transverse Fuel Injection***, in *Computational Fluid Dynamics Symposium on Aeropropulsion*, NASA-CP-3078, pages 635–667, NASA, Cleveland, OH (Apr. 1990).

[10] Portz, R. and Segal, C., ***Penetration of Gaseous Jets in Supersonic Flows***, AIAA J., 44(10):2426–2429 (Oct. 2006).

[11] Riggins, D. W., McClinton, C. R., and Vitt, P. H., ***Thrust Losses in Hypersonic Engines Part 1: Methodology***, J. Propul. Power., 13(2):281–287 (1997).

[12] VULCAN-CFD, ***http://vulcan-cfd.larc.nasa.gov/*** (Dec. 2017).

[13] van Leer, B., ***Towards the Ultimate Conservative Difference Scheme. V: A Second-Order Sequel to Godunov's Method***, J. Comput. Phys., 32(1):101–136 (Jul. 1979).

[14] Edwards, J. R., ***A Low-Diffusion Flux-Splitting Scheme for Navier-Stokes Calculations***, Comput. Fluids., 26(6):635–659 (Jul. 1997).

[15] McBride, B. J., Gordon, S., and Reno, M. A., ***Thermodynamic Data for Fifty Reference Elements***, NASA Technical Paper 3287/REV1, NASA, Cleveland, OH (Feb. 2001).

[16] Pulliam, T. H. and Chaussee, D. S., ***A Diagonal Form of an Implicit Approximate-Factorization Algorithm***, J. Comput. Phys., 39(2):347–363 (Feb. 1981).

[17] Menter, F. R., ***Two-Equation Eddy-Viscosity Turbulence Models for Engineering Applications***, AIAA J., 32(8):1598–1605 (Aug. 1994).

[18] Ó Conaire, M., Curran, H. J., Simmie, J. M., Pitz, W. J., and Westbrook, C., ***A Comprehensive Modeling Study of Hydrogen Oxidation***, Int. J. Chem. Kinet., 36(11):603–622 (2004).

[19] Wilcox, D. C., ***Turbulence Modeling for CFD***, DCW Industries, Inc., La Cañada, CA (2000).

[20] Adams, B., Ebeida, M., Eldred, M., Geraci, G., Jakeman, J., Maupin, K., Monschke, J., Stephens, J., Swiler, L., Vigil, D., Wildey, T., Bohnhoff, W., Dalbey, K., Eddy, J., Frye, J., Hooper, R., Hu, K., Hough, P., Khalil, M., Ridgway, E., Winokur, J., and Rushdi, A., ***DAKOTA, A Multilevel Parallel Object-Oriented Framework for Design Optimization, Parameter Estimation, Uncertainty Quantification, and Sensitivity Analysis: Version 6.8 User's Manual***, Sandia Technical Report SAND2014-4633, Sandia (May 2018).

[21] Drayna, T., Haag, C., Bartkowicz, M., and Gidzak, V., ***LINK3D***, Software package, version 1.0.0, GoHypersonic, Inc. (2016).